Journal of Fluids and Structures 140 (2026) 104449

Contents lists available at ScienceDirect

Journal of Fluids and Structures

journal homepage: www.elsevier.com/locate/jfs

Energy harvesting from vortex-induced vibrations using a pendulum

F.J. Huera-Huarte

Department of Mechanical Engineering, Universitat Rovira i Virgili., 43007 Tarragona, Spain

ARTICLE INFO

Keywords:
Vortex-induced vibrations
Energy harvesting

ABSTRACT

This paper presents an experimental investigation into energy harvesting from vortex-induced vibrations (VIV) using a pendulum-based arrangement. A series of experiments were conducted in a water channel to examine the effects of flow velocity and applied braking torque on the pendulum shaft. The motion of the pendulum and the fluid loading were measured and analyzed to assess the power output and dynamic response of the system under varying flow and braking conditions. Results indicate that energy extraction is maximized within a narrow range of flow velocities that induce lock-in response, particularly for the highest braking torques that allow motion on the system. A constant (limited) braking torque was applied to evaluate mechanical power at the shaft, and while the braking function was not optimized, the study demonstrates that the system can achieve energy conversion efficiencies comparable to other VIV-based energy harvesting configurations.

1. Introduction

The increasing global demand for sustainable energy has driven significant interest in alternative energy harvesting technologies. As concerns over environmental sustainability grow, researchers seek innovative methods to harness renewable energy from environmental forces. Among these, energy harvesting from fluid-elastic instabilities, has emerged as a promising technique for converting hydrokinetic fluid flow energy into usable electrical energy (Abdelkefi, 2016; Ma and Zhou, 2022).

Among the various fluid-elastic phenomena, vortex-induced vibration (VIV) has attracted considerable attention due to its potential for energy conversion. VIV occurs when fluid flow past a bluff body induces oscillatory forces, leading to periodic motion (Blevins, 1990; Williamson and Govardhan, 2004; Bearman, 2011; Huera-Huarte, 2025). The idea of utilizing VIV as a viable mechanism for energy conversion is not new, it was first introduced by Bernitsas et al. (2008). This group has developed and characterized, over the last two decades, a system based on the translational VIV motion of a one degree of freedom elastically mounted rigid cylinder (Bernitsas et al., 2009; Park et al., 2013; Sun et al., 2016; Zhang et al., 2018). Other systems constrain the motion of the one degree-of-freedom model along a circular trajectory using a pivoting arm, with the whole cylinder acting as a horizontal pendulum (Arionfard and Nishi, 2017; Malefaki and Konstantinidis, 2020). Despite the success of one degree-of-freedom VIV harvesters, challenges remain in optimizing their adaptability to varying flow conditions, as their applicability is conditioned by the narrow range of VIV locked-in response (Barrero-Gil et al., 2012; Han et al., 2023). In response to these challenges, recent studies have explored alternative systems for VIV energy harvesting, including the use of flexible cylinders (Grouthier et al., 2014; Antoine et al., 2016). These systems exhibit multiple lock-in states (Huera-Huarte, 2025), thereby expanding the range of conditions under which energy harvesting can occur. However, in terms of practical applicability, flexible systems present a significant challenge, the placement of the energy harvester. The complex motion resulting from VIV can make integration and efficiency maximization particularly difficult.

E-mail address: francisco.huera@urv.cat.

https://doi.org/10.1016/j.jfluidstructs.2025.104449
Received 4 March 2025; Received in revised form 27 October 2025; Accepted 31 October 2025

Available online 6 November 2025
0889-9746/© 2025 The Author. Published by Elsevier Ltd. This is an open access article under the CC BY-NC-ND license (http://creativecommons.org/licenses/by-nc-nd/4.0/).

A pendulum system offers distinct advantages, including design simplicity and tuneability. The majority of the engineering components required to convert energy can be placed outside the water, with the cylinder itself being the only part exposed to the current. This configuration simplifies maintenance and minimizes exposure to harsh environments. Additionally, the rotary motion of the pendulum makes it easier to integrate with generator systems for energy conversion. On the contrary, pendulums are characterized by yielding linear amplitude variations as they oscillate, compared to the uniform amplitude distribution in classical one degree of freedom arrangements. Not only that, but their flow dynamics and vortex shedding are expected to be more complex. The literature describing the VIV dynamics of pendulums in uniform cross-flow is not abundant, and some of the first works describing their response are those by Balasubramanian et al. (2000) and Flemming and Williamson (2005). Recent works have focused on describing numerically the response of two degree-of-freedom pivoted systems (Cajas et al., 2021, 2023).

Although several studies have investigated vortex-induced vibrations (VIV) in pendulum systems, experimental research on this topic remains relatively limited. This gap is even more pronounced in the case of pendulum-based energy harvesters, where a deeper understanding of fluid–structure interactions, dynamic response, and efficiency is still needed to advance towards practical applications. For example, in the work of Kim et al. (2018), the authors considered harvesting applications; however, their study primarily focused on describing experimentally the dynamics of a pendulum system without analyzing its energy harvesting performance. To address these gaps, the present study explores, using experiments, an energy harvesting system based on a pendulum configuration in cross-flow. Rather than employing a specific energy conversion device, a controllable braking system is implemented to directly measure its mechanical power output. This approach ensures the experiments remain general and adaptable to various energy harvesting mechanisms.

The paper is structured as follows: first, we describe the experimental set-up and the main governing parameters. Next, we present the dynamic response of the system without any applied braking torque. Finally, we analyze the power output capabilities of the system, by applying different levels of constant braking torque to the pendulum's shaft. The optimization of the braking function – specifically, the dynamic variation of the applied torque to maximize power output – is beyond the scope of this study and will be explored in future experiments.

2. Experimental methods

A series of experiments were conducted in the free-surface water channel at the Laboratory for Fluid-Structure Interaction at Universitat Rovira i Virgili. The channel features a glass-walled working section with a cross-sectional area of approximately 1×1 m^2, located downstream of a three-dimensional contraction. The flow profile in this section exhibits minimal velocity fluctuations, with a maximum spatio-temporal variability of less than 1.6%, and a turbulence intensity (root mean square of the velocity upon its mean) of 2.8% at the highest free stream velocity configured in the channel.

The experimental set-up comprises a pendulum arrangement consisting of a main shaft, an aluminum profile, and a circular cylinder model. The main shaft, made from an aluminum pipe with a 25 mm external diameter, is supported by two air-bearing blocks attached to a structure that positions the entire set-up above the water channel, with the shaft parallel to the flow direction. The aluminum profile is rigidly connected to the main shaft and provides attachment points for two springs with stiffness constant k. The air bearings ensure negligible friction within the pendulum arrangement. The cylinder model used in the experiments is made of a translucent acrylic pipe with an external diameter D of 50 mm, also rigidly connected to the main shaft. The total length of the pendulum, measured from its bottom end to the center of the main shaft, L_t, is 720 mm. While the main shaft, air bearings, profile, and springs are positioned outside the water, a length L of 620 mm of the cylinder remains exposed to the current in the water channel. The entire rotating assembly – including the shaft, profile, and cylinder – has a total mass m_a of 1.21 kg.

A contactless laser sensor measures the oscillations of the profile near one of its ends, enabling the computation of the oscillation angle of the cylinder, θ. An electro-magnetic powder brake (EMPB) is mounted on the supporting structure and coupled to the main shaft via a torque measurement sensor and custom adaptor parts designed for these experiments. The electromagnetic powder brake uses magnetic powder and an electromagnetic force to generate a highly controllable resistive torque. It produces minimal friction when inactive, as the powder is dispersed (at 10 rad/s the damping coefficient of the brake would approximately 0.004 Nms/rad, therefore negligible). When current flows through the stator coil, a magnetic field forms, causing the powder to align and resist rotation. The torque increases with current, offering precise control and fast response, therefore allowing the application of different levels of torque to the main shaft, using a power supply governed by a precision potentiometer. Fig. 1a presents a three-dimensional representation of the experimental setup, along with a cross-sectional schematic in 1b. For clarity, the supporting structure, which holds the brake and air bearings, is omitted from the figure.

Fig. 1c presents the results of a decay test conducted in air, showing both the temporal evolution of the angle θ and the spectrum of the temporal signal. The damping ratio ξ, which characterizes the exponential decay in free oscillation tests, was determined to be around 9% of the critical damping. With this very low damping, the dominant frequency observed in the spectrum in Fig. 1c, with a value of 1.57 Hz, can be considered nearly equal to the natural frequency of the system in air f_{n_a} (since $\sqrt{1-\xi^2}$=0.996).

3. Theoretical description of the problem and dimensionless parameters

In this section we consider the undamped forced oscillations of the one degree-of-freedom pendulum arrangement described previously. In such a system, if a harmonic fluid excitation of the form $M_F(t) = M_{F_o}\sin(2\pi f_s t+\phi)$, is assumed, the dynamic response results in a harmonic function of the form $\theta(t) = \theta_o \sin(2\pi f_s t)$, with ϕ being the phase difference between excitation and response. The external loads acting on the system (see Fig. 1b for an schematic view of the problem) are caused by the incoming fluid (M_F),

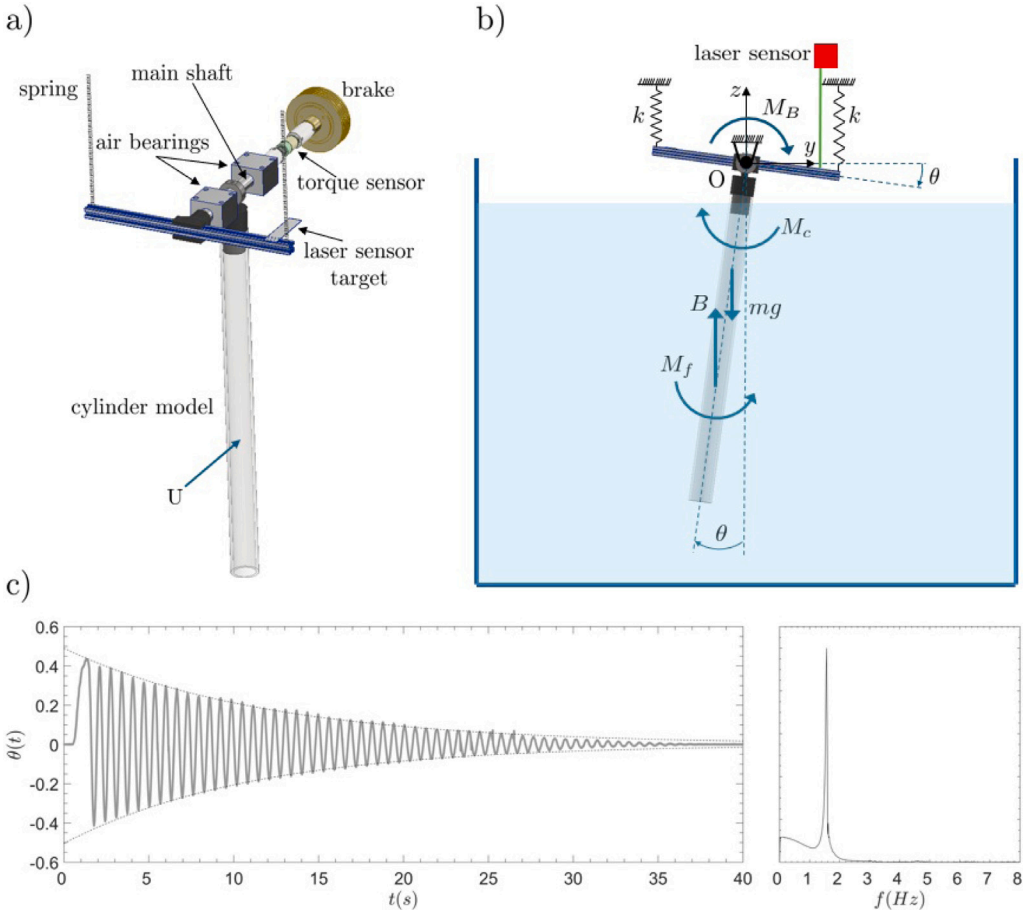


Fig. 1. (a) Three dimensional representation of the experimental set-up. The brake and the air bearings are attached to a supporting structure not shown for the sake of clarity. (b) Cross-sectional schematic of the experimental set-up. (c) Results of a decay test in air showing the amplitude of oscillations (θ) with the exponential decay envelopes and the spectrum of the signal.

damping (M_c), gravity (mg), buoyancy (B) and the brake (M_B). The equation of motion can be obtained using Newton's second law in moment form, $\sum_i M_i^{ext} = I_O\ddot{\theta}$, which states that the summation of all external moments applied to the system is equal to the total inertia respect to the main rotation shaft (I_O), times the angular acceleration ($\ddot{\theta} = \frac{d^2\theta}{dt^2}$) of the system. For small amplitude oscillations, the non-linear terms can be linearized, leading to Eq. (2).

$$I_O\ddot{\theta} + M_c + M_k + M_B = M_F \tag{1}$$

where the stiffness term being $M_k = \left(2kd_1^2 + mgd_2 - m_v g d_3\right)\theta$ and the dissipation term $M_c = (c_{O_s} + c_{O_f})\dot{\theta}$. In the expressions, k is the stiffness constant of the springs, d_1 is the distance from the axis O to the attachment point of the springs in the aluminum profile, d_2 is the distance from O to the center of mass of the system, d_3 is the distance from O to the center of buoyancy of the cylinder and g is the acceleration of gravity. The mass m results from the oscillating mass of the system in air (m_a) plus the added or virtual mass (m_v), that can be computed using the expression $C_a\rho\pi D^2 L/4$, with C_a being the added mass coefficient, in this case equal to 1. The fluid density is ρ. The inertia of the system (I_O) results from the inertia of the rotating parts of the system in air (I_{O_a}), plus the added or virtual inertia (I_{O_v}) that can be computed by means of expression $C_a(m_v L^2/12 + m_v d_3^2)$. The dissipation results from the structural (c_{O_s}) and fluid damping (c_{O_f}) coefficients and the angular velocity ($\dot{\theta} = \frac{d\theta}{dt}$) of the system. Structural damping can be neglected because the system rotates in the air bearing rig, ensuring no friction losses and the unloaded EMPB generates very small frictional torque, as commented before. Eq. (1) results in,

$$I_O\ddot{\theta} + \left(2kd_1^2 + mgd_2 - m_v g d_3\right)\theta + M_B = M_f \tag{2}$$

Note that M_f includes not only the fluid force but also the fluid damping term. The natural frequency of the system in water is,

$$f_n = \frac{1}{2\pi}\sqrt{\frac{2kd_1^2 + mgd_2 - m_v g d_3}{I_O}} \tag{3}$$

whereas in air, without including buoyancy and added mass effects, it results in,

$$f_{n_a} = \frac{1}{2\pi}\sqrt{\frac{2kd_1^2 + m_a g d_2}{I_{O_a}}} \tag{4}$$

Introducing the experimental values in these two expressions, one obtains f_n=0.79 Hz and f_{n_a}=1.57 Hz. Experimental decay tests in water result in a frequency of 0.75 Hz and in air of 1.57 Hz (presented in Fig. 1c).

For this work, the brake is configured to apply a constant torque with different magnitudes. A constant torque here means the current applied to the EMPB is limited to a certain value. As the system is moving with angular velocity $\dot{\theta}$, the torque M_B ends up being a time varying function where the value of the braking torque oscillates between a positive and negative torque plateau, approximately as in a square signal. The imposed current to the EMPB (torque function) is not optimized for energy harvesting, but it allows the characterization of the system under the most immediate and practical torque conditions. Future experiments will be conducted using other torque functions to study the optimal energy harvesting capabilities of the system.

During the experiments the temporal evolution of θ and M_B, are measured using the laser and the torque sensors described in Section 2, therefore, the fluid loading M_f can be computed using Eq. (2), providing an estimation of the fluid loading acting on the system.

Dimensional analysis results in a set of dimensionless parameters that can be used to characterize the system. These are mass ratio ($m^* = m_a/m_v$), combined mass-damping parameter ($m^*\xi$), inertia ratio ($I_O^* = I_{O_a}/I_{O_v}$), Strouhal number ($S = f_s U/D$), reduced velocity ($U^* = U/f_n D$), Reynolds number ($Re = \rho U D/\mu$) and brake torque coefficient ($C_B = 2M_B/(\rho U^2 L^2 D)$). The measurement of θ allows to compute the dimensionless tip amplitude ratio $A^* = \theta_o L_t/D$, where θ_o results from the average of the peaks observed each cycle in the oscillation during each experiment, and the frequency ratio $f^* = f/f_n$, where f is the dominant frequency observed in each experiment after Fourier analysis. The fluid moment coefficient $C_{M_f} = 2\tilde{M}_f/(\rho U^2 L^2 D)$, is computed using the RMS value of the fluid loading ($\tilde{M}_f$). In the cases with the brake applying a torque on the system, the mechanical power available at the shaft, can be computed as the product of the measured torque and the angular velocity, $P(t) = M_b(t)\dot{\theta}(t)$, that can be expressed in dimensionless form as the power coefficient $C_P = 2\tilde{P}/(\rho U^3 L D)$, using the RMS value of the power ($\tilde{P}$) .

4. Vortex-induced vibrations of the pendulum arrangement

The first set of tests was carried out with the EMPB not working, i.e with only the negligible residual torque of the brake applied to the system. With this configuration, the free stream flow velocity in the water channel was varied in small steps, yielding variations in U^* and Re in the range from approximately 5 to 12 and from 9000 to 21000, respectively. At each free stream velocity, θ and M_B were measured using a sampling rate of 2 kHz, during at least 60 s, therefore, acquiring a large number of oscillation cycles. A series of initial tests and trials revealed that under the smallest reduced velocity presented in the results, the application of a very small torque resulted in the disappearance of VIV, that is why experiments were focused on the analysis of the lock-in region, and why reduced velocities smaller than 5 or larger than 12 were not considered. Moreover, by doing this, the total number of experiments to conduct, was reduced considerably.

The results of a typical experiment, for U^*=5.8 (Re=10130), appear in Fig. 2. In the upper row (plot 2a) the time series (20 s) of the dimensionless tip displacement of the cylinder $A^*(t)$, appears together with the mean value of the positive and negative peaks A^*, indicated with the dashed lines. In plot 2b the averaged cycle of the amplitude is plotted as a function of dimensionless time ($t^* = tf$), using a thick black line on top of all the individual cycles in the experiment (gray lines). This phase-averaged data has been obtained after breaking the signal into individual cycles (identifying the start and the end of each cycle in each experiment) and time-averaging the ordered data, sample by sample, to obtain the averaged cycle. The spectrum of the times series is shown in 2c. The second row is for the fluid loading, with the time series of the fluid force coefficient $C_{M_f}(t)$, in plot 2d. The horizontal dotted line indicates the RMS value of the coefficient. In 2e the fluid loading averaged cycle is presented, and the spectrum appears in 2f.

The results obtained by varying the free-stream velocity in the water channel – i.e., varying U^* and Re – without brake actuation are presented in Fig. 3. The amplitude data (Fig. 3a) exhibits the characteristic VIV locked-in response of a cylinder, with peak amplitudes occurring at reduced velocities near 6, followed by a gradual decay as the system transitions through the desynchronization range. The amplitude levels observed in the lock-in and desynchronization branches, are similar to those reported by Flemming and Williamson (2005), even though their pendulum had two degrees of freedom. In the experiments by Kim et al. (2018), with varying stiffness and aspect ratio, authors only report amplitudes, and for their longer aspect ratio, amplitudes are very similar. The frequency response shows that the oscillation frequencies closely follow the excitation, remaining near the system's natural frequency in water, with f^* ranging approximately from 0.8 to 1.3 inside the lock-in range.

As seen in Fig. 3c, the maximum amplitudes correspond to high fluid force coefficients that are in phase with the motion (Fig. 3d). These coefficients rapidly decrease through the desynchronization branch, leading to a phase jump at a reduced velocity of approximately 7, where motion and loading become out of phase.

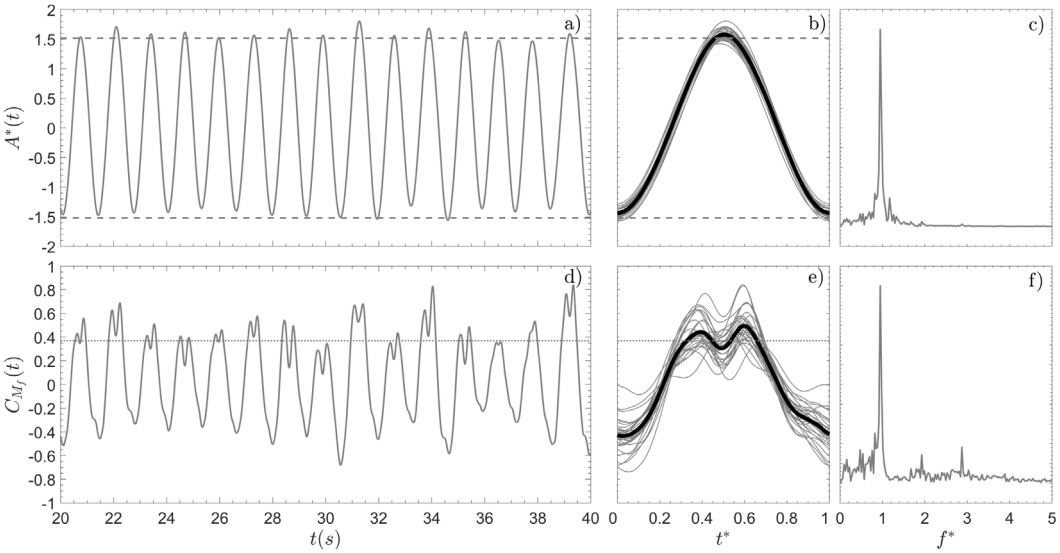


Fig. 2. Measurements obtained in an experiment conducted without brake actuation, at a reduced velocity U^* of 5.8 and a Reynolds number Re of 10130. Plot (a) in the first row, shows the time series of the dimensionless tip displacement of the cylinder (A^*) and plot (b) shows the phase-averaged cycle of the same magnitude, together with the spectrum in plot (c). In the second row, plots (d), (e) and (f) show the time series, the phase-averaged cycle and the spectrum of the coefficient of fluid loading C_{M_f}.

5. Limited constant torque applied to the system for energy harvesting

This section presents results for cases where the brake applies different limited constant torque levels to the system's main shaft. Measuring this torque allows for the computation of the mechanical power available at the shaft, as discussed in Section 3. The system's response varies significantly depending on the applied braking torque. A typical experiment, conducted at a reduced velocity U^* of 11.2 and a Reynolds number Re of 19490, outside the upper branch, appears in Fig. 4. In plot 4a the time series of the dimensionless tip amplitude (A^*) appears plotted besides the its phase-averaged cycle in plot 4b. The spectrum is presented in plot 4c. The dashed line indicates the computed A^* for this run. The time series, the averaged cycle and the spectrum of the coefficient of fluid loading C_{M_f} are shown in plots 4d to 4f. The third row, with plots 4g to 4i, is for the measured braking torque C_B, its averaged cycle and its spectrum. In the first two plots of the row, the dotted line indicates the C_B obtained for this run, computed from the average value in the plateaus of the averaged cycle. Finally, in the last row, plots 4j to l, are for the time evolution of the power coefficient (C_P), its phase-averaged cycle and its spectrum. Dotted lines in plots 4d, e, j and l indicate computed RMS values for this run.

Fig. 5 shows a series of plots with the same structure described for Fig. 4, but for a case that falls inside the upper branch (U^*=5.2 and Re=9090), where the largest oscillations of the cylinder were observed. This case is prototypical of the cases that yield the largest power output in the shaft of the system. Oscillations are highly periodic without amplitude modulation as in the case of Fig. 4. The applied torque coefficient and the estimated fluid torque coefficient are not as similar as they were in the other case. The measured C_B is very close to be a square signal with very well defined plateaus (positive and negative) where the torque is almost constant.

The results from over 150 experiments conducted with varying levels of constant torque applied to the system are presented in Fig. 6. Lighter colors represent higher applied torque magnitudes as indicated by the colorbar in the figure. At the highest torque levels, the cylinder exhibits oscillations only at reduced velocities above 7.1 (Fig. 6a). At the highest reduced velocities, oscillation amplitudes range from $0.5D$ for maximum torque to $1.15D$ for zero applied torque.

Dimensionless frequencies (Fig. 6b) remain mostly unchanged at reduced velocities below 7 but shift noticeably at higher velocities under applied torque. Fluid loading on the cylinder (Fig. 6c) also varies with torque, particularly within the U^* range of 6.5 to 9.5. The most significant effect of braking torque is observed in the phase difference (Fig. 6d). Without torque, a sudden phase shift occurs around $U^* \approx 7$, whereas at higher torque levels, the phase transitions smoothly from approximately 60 to 90 degrees.

The amplitude A^* data presented in Fig. 6a, appears plotted in a colormap in (Fig. 7), together with the fluid loading coefficient C_{M_f} in Fig. 7b, both as a function of the brake torque C_B applied and reduced velocity U^*. In Fig. 7c, the power coefficient (C_P) is presented. The largest power coefficients, and therefore the largest power available in the shaft for energy harvesting, take place when the applied torque is large but not enough to completely reduce oscillations. The region of high power coefficient correlates well with the region where the highest fluid loading is produced, in a narrow band of reduced velocities from around 5.5 to 6.5, for the largest applied C_B. Note that the objective of this work was not to analyze the effects of different braking functions on

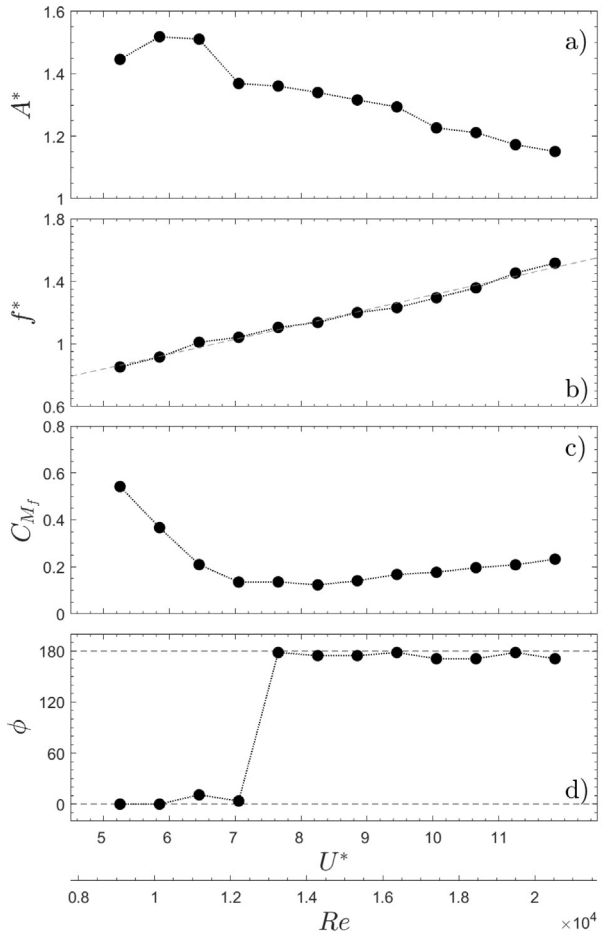


Fig. 3. Results for the experiments without brake actuation as a function of U^* and Re. Plot (a) depicts dimensionless tip amplitudes (A^*) and plot (b) dimensionless response frequencies (f^*). Plots (c) and (d) are for the root mean square value of the fluid loading coefficient (C_{M_f}) and the phase difference between loading and response (ϕ).

the available mechanical power, though it is expected that an optimal torque function exists for maximizing the mechanical power output per cycle. Future studies will focus on this aspect, where the applied torque will be actively controlled based on fluid loading or the system's angular position to enhance energy harvesting efficiency.

The data presented here demonstrates that even a non-optimized system can achieve C_P values exceeding 0.1 across a wide range of flow conditions, provided the applied constant torque C_B remains inside the range [0.15, 0.25]. Although significant efficiencies are limited to a narrow response band, this region could be enlarged by the appropriate control of braking and by adapting the length or mass distribution of the system. In flexible systems, this is not needed because of the inherent type of response of cables, where lock-in states are always present. The peak values obtained here ($C_{P_{max}} = 0.16$), are comparable to those obtained with other different harvesting configurations (Grouthier et al., 2014; Antoine et al., 2016). The VIVACE energy converter, which operates based on a translational degree of freedom (DOF), has been reported to achieve energy conversion efficiencies of approximately 0.22, with peak values reaching 0.30 (Bernitsas et al., 2009). These values are generally higher than those reported in other studies, including the present work. For instance, the one-degree-of-freedom (1 DOF) translational system investigated by Han et al. (2023) demonstrated efficiencies up to 0.16. Similarly, Barrero-Gil et al. (2012) reported efficiencies ranging from 0.05 to 0.15 for 1 DOF translational systems, with variations depending on the Reynolds number and the level of damping applied.

6. Conclusions

The hydrokinetic VIV energy harvesting potential of a one-degree-of-freedom pendulum configuration has been studied in detail. In this initial phase of the work, a limited constant amplitude braking torque function was employed, which has demonstrated energy harvesting capabilities similar to other VIV configurations. It is likely that these capabilities can be significantly improved through the use of optimized braking functions, or even using upstream wake interference, aspects that will be studied in future works.

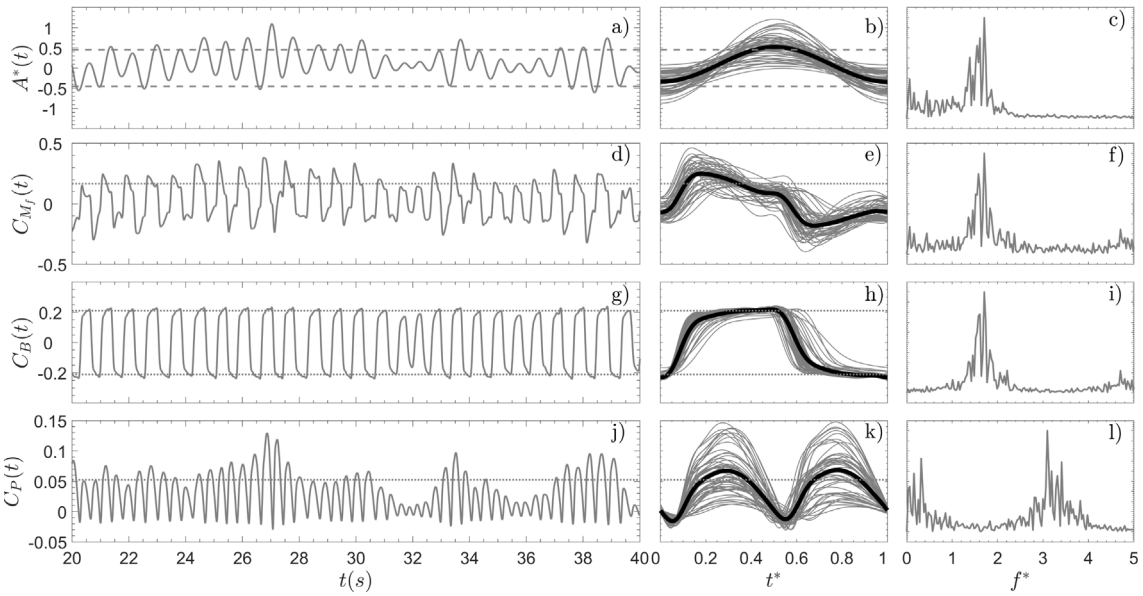


Fig. 4. Measurements obtained in an experiment conducted without brake actuation, at a reduced velocity U^* of 11.2 and a Reynolds number Re of 19490. Plot (a) in the first row, shows the time series of the dimensionless tip displacement of the cylinder (A^*) and plot (b) shows the phase-averaged cycle of the same magnitude, together with the spectrum in plot (c). In the second row, plots (d), (e) and (f) show the time series, the phase-averaged cycle and the spectrum of the coefficient of fluid loading C_{M_f}. In the last row, plots (g), (h) and (i) the coefficient of power (C_P), its cycled average magnitude and its spectrum, are shown.

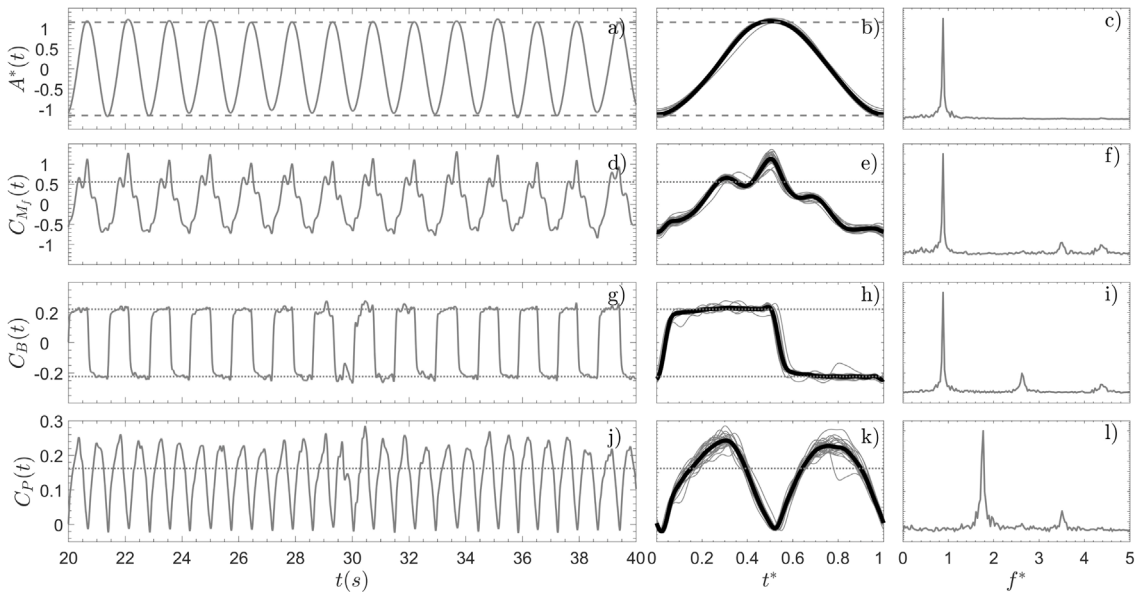


Fig. 5. Measurements obtained in an experiment conducted without brake actuation, at a reduced velocity U^* of 4.5 and a Reynolds number Re of 9090. Plot (a) in the first row, shows the time series of the dimensionless tip displacement of the cylinder (A^*) and plot (b) shows the phase-averaged cycle of the same magnitude, together with the spectrum in plot (c). In the second row, plots (d), (e) and (f) show the time series, the phase-averaged cycle and the spectrum of the coefficient of fluid loading C_{M_f}. In the last row, plots (g), (h) and (i) the coefficient of power (C_P), its cycled average magnitude and its spectrum, are shown.

Although the pendulum-based configuration presented here has received practically no research attention, this study highlights the need for further studies to fully explore its potential.

The highest energy harvesting capabilities were observed with the largest braking torques that allowed motion on the system, which correlate strongly with the highest fluid loading acting on the cylinder. In terms of frequency response, the harvesting is

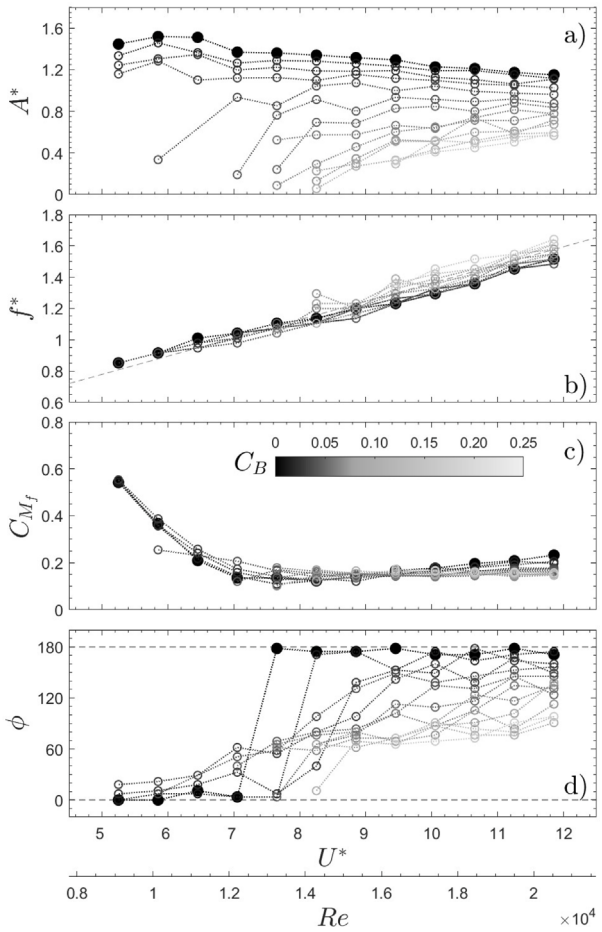


Fig. 6. Dimensionless tip amplitudes A^* (a), frequencies f^* (b), fluid loading coefficients C_{M_f} (c) and phase differences ϕ (d), as a function of reduced velocity U^* or Re and applied braking torque C_B. The lighter color, the higher the braking torque applied.

constrained to a narrow frequency range around reduced velocities of approximately 6, where typical locked-in responses occur, showing C_Ps well over 0.1.

From a practical application perspective, the pendulum configuration provides a key advantage: it allows critical components – including the shaft, the generator, and the supporting structures – to be positioned outside the water, with only the cylinder penetrating the free surface, simplifying engineering design and maintenance. It also allows for relatively easy adjustment of the natural frequency by altering the mass distribution (rotational inertia) and/or cylinder length, making the widening of the response band feasible. Future research will explore this concept further, focusing on passive solutions based on the control of hydrodynamic forces acting on the cylinder.

Declaration of competing interest

The authors declare that they have no known competing financial interests or personal relationships that could have appeared to influence the work reported in this paper.

Acknowledgments

The author would like to acknowledge the funding provided by the Spanish Agencia Estatal de Investigación through grant PID2021-128441NB-I00.

Data availability

Data will be made available on request.

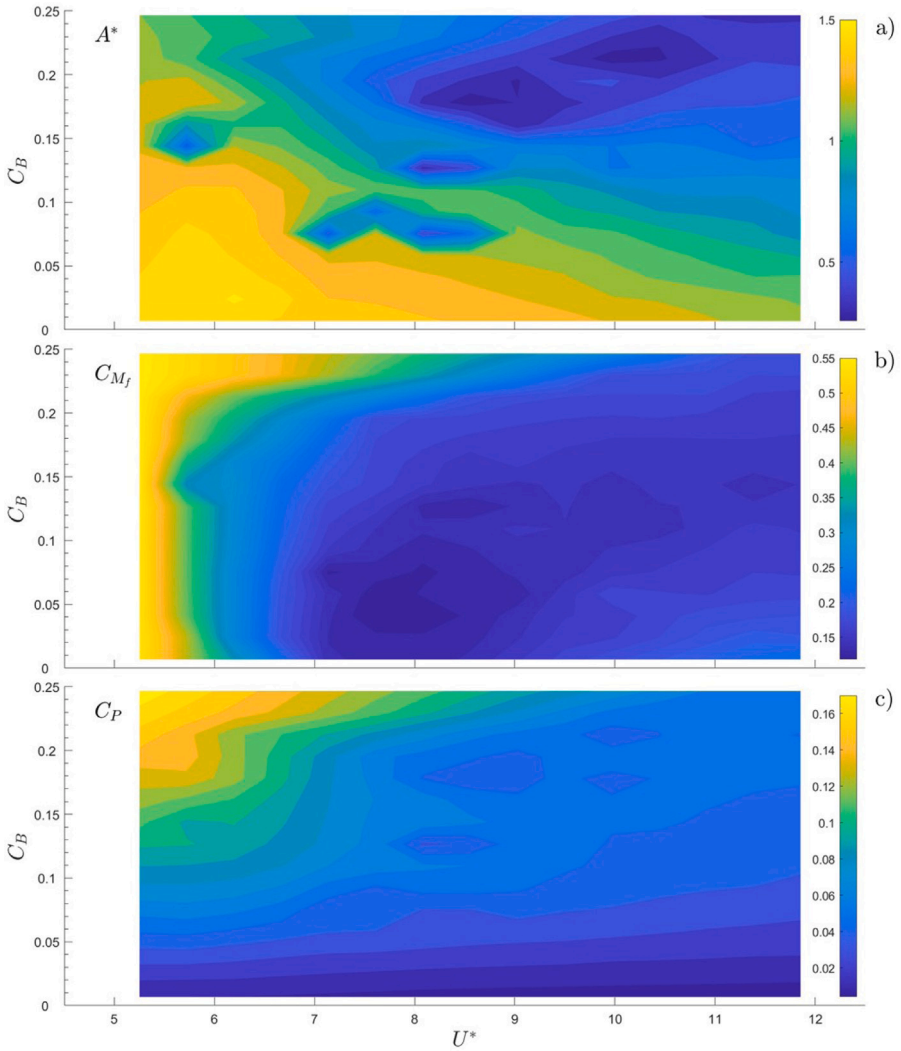


Fig. 7. Dimensionless tip amplitude A^* (a), fluid loading coefficient C_{M_f} (b) and power coefficient C_P (c), as a function of brake torque coefficient C_B and reduced velocity U^*.

References

Abdelkefi, A., 2016. Aeroelastic energy harvesting: A review. Internat. J. Engrg. Sci. 100, 112–135.

Antoine, G.O., de Langre, E., Michelin, S., 2016. Optimal energy harvesting from vortex-induced vibrations of cables. Proc. R. Soc. A: Math. Phys. Eng. Sci. 472, 20160583.

Arionfard, H., Nishi, Y., 2017. Experimental investigation of a drag assisted vortex-induced vibration energy converter. J. Fluids Struct. 68, 48–57.

Balasubramanian, S., Skop, R.A., Haan, F.L., Szewczyk, A.A., 2000. Vortex-excited vibration of uniform pivoted cylinders in uniform and shear flow. J. Fluids Struct. 14, 65–85.

Barrero-Gil, A., Pindado, S., Avila, S., 2012. Extracting energy from vortex-induced vibrations: A parametric study. Appl. Math. Model. 36, 3153–3160.

Bearman, P., 2011. Circular cylinder wakes and vortex-induced vibrations. J. Fluids Struct. 27 (5–6), 648–658.

Bernitsas, M.M., Ben-Simon, Y., Raghavan, K., Garcia, E.M., 2009. The VIVACE converter: Model tests at high damping and reynolds number around 105. J. Offshore Mech. Arct. Eng. 131.

Bernitsas, M.M., Raghavan, K., Ben-Simon, Y., Garcia, E.M., 2008. VIVACE (vortex induced vibration aquatic clean energy): A new concept in generation of clean and renewable energy from fluid flow. J. Offshore Mech. Arct. Eng. 130.

Blevins, R., 1990. Flow-Induced Vibration. Van Nostrand Reinhold.

Cajas, J.C., Pastrana, D., Rodríguez, I., Lehmkuhl, O., Houzeaux, G., Vázquez, M., Treviño, C., 2021. Vortex induced vibrations of a pivoted finite height cylinder at low Reynolds number. Phys. Fluids 33.

Cajas, J.C., Rodríguez, I., Salcedo, E., Lehmkuhl, O., Houzeaux, G., Treviño, C., 2023. Aspect ratio influence on the vortex induced vibrations of a pivoted finite height cylinder at low Reynolds number. Phys. Fluids 35.

Flemming, F., Williamson, C.H., 2005. Vortex-induced vibrations of a pivoted cylinder. J. Fluid Mech. 522, 215–252.

Grouthier, C., Michelin, S., Bourguet, R., 2014. On the efficiency of energy harvesting using vortex-induced vibrations of cables. J. Fluids Struct. 49, 427–440.

Han, P., Huang, Q., Pan, G., Qin, D., Wang, W., Gonçalves, R.T., Zhao, J., 2023. Optimal energy harvesting efficiency from vortex-induced vibration of a circular cylinder. Ocean Eng. 282.
Huera-Huarte, F., 2025. Vortex-induced vibration of flexible cylinders in cross-flow. Annu. Rev. Fluid Mech. 57, 285–310.
Kim, J., Song, M., Kim, D., 2018. Large-amplitude flow-induced vibration of cylindrical pendulums. J. Fluids Struct. 79, 39–49.
Ma, X., Zhou, S., 2022. A review of flow-induced vibration energy harvesters. Energy Conv. Manag. 254, 115223.
Malefaki, I., Konstantinidis, E., 2020. Assessment of a hydrokinetic energy converter based on vortex-induced angular oscillations of a cylinder. Energies 13, 717–730.
Park, H., Kumar, R.A., Bernitsas, M.M., 2013. Enhancement of flow-induced motion of rigid circular cylinder on springs by localized surface roughness at $3 \times 10^4 \leq Re \leq 1.2 \times 10^5$. Ocean Eng. 72, 403–415.
Sun, H., Kim, E.S., Nowakowski, G., Mauer, E., Bernitsas, M.M., 2016. Effect of mass-ratio, damping, and stiffness on optimal hydrokinetic energy conversion of a single, rough cylinder in flow induced motions. Renew. Energy 99, 936–959.
Williamson, C., Govardhan, R., 2004. Vortex-Induced Vibrations. Annu. Rev. Fluid Mech. 36 (1), 413–455.
Zhang, D., Sun, H., Wang, W., Bernitsas, M.M., 2018. Rigid cylinder with asymmetric roughness in flow induced vibrations. Ocean Eng. 150, 363–376.